



## RESEARCH LETTER

10.1002/2013GL058476

## Key Points:

- Ambient noise adjoint tomography refines the SE Tibet crustal model
- The mid-lower crust shows stronger wavespeed reduction (6 - 12%)
- Mapped low wavespeed zones suggest crustal flow confined by stable regions

## Supporting Information:

- Readme

## Correspondence to:

M. Chen,  
min.chen@rice.edu

## Citation:

Chen, M., H. Huang, H. Yao, R. van der Hilst, and F. Niu (2014), Low wave speed zones in the crust beneath SE Tibet revealed by ambient noise adjoint tomography, *Geophys. Res. Lett.*, *41*, 334–340, doi:10.1002/2013GL058476.

Received 29 OCT 2013

Accepted 20 DEC 2013

Accepted article online 23 DEC 2013

Published online 22 JAN 2014

## Low wave speed zones in the crust beneath SE Tibet revealed by ambient noise adjoint tomography

Min Chen<sup>1,2</sup>, Hui Huang<sup>1</sup>, Huajian Yao<sup>1,3</sup>, Rob van der Hilst<sup>1</sup>, and Fenglin Niu<sup>2,4</sup>

<sup>1</sup>Department of Earth and Planetary Sciences, Massachusetts Institute of Technology, Cambridge, Massachusetts, USA,

<sup>2</sup>Department of Earth Science, Rice University, Houston, Texas, USA, <sup>3</sup>Laboratory of Seismology and Physics of Earth's Interior, School of Earth and Space Sciences, University of Science and Technology of China, Hefei, Anhui, China, <sup>4</sup>State Key Laboratory of Petroleum Resource and Prospecting, and Unconventional Natural Gas Institute, China University of Petroleum, Beijing, China

**Abstract** We present a refined 3D crustal model beneath SE Tibet from ambient noise adjoint tomography. Different from ray-theory-based tomography, adjoint tomography in this study incorporates a spectral-element method (SEM) and takes empirical Green's functions (EGFs) of Rayleigh waves from ambient noise interferometry as the direct observation. The frequency-dependent traveltimes misfits between SEM synthetic Green's functions and EGFs are minimized with a preconditioned conjugate gradient method, meanwhile the 3D model gets improved iteratively utilizing 3D finite-frequency kernels. The new model shows 3 – 6% shear wave speed increasing beneath the western Sichuan Basin (SCB) (depth > 15 km) and the central Chuan-Dian Block (CDB), and 6 – 12% shear wave speed reduction in the mid-lower crust beneath the northern and the southern CDB. The inferred spatial pattern of low wave speed zones, consistent with possible partial melt, suggests more complex and disconnected geometry than the pervasive narrow zone from the channel flow models.

### 1. Introduction

India-Eurasia collision created the Himalaya-Tibet orogen with its vicinity undergoing complex deformation. Two types of models, assuming different lithosphere rheology at depth, have been used to explain the clockwise rotation of SE Tibet around the eastern Himalayan syntaxis: (1) the first model requires rigid lithospheric blocks segmented by large-scale strike slip faults and, probably, strong crust-mantle lithosphere coupling [Tapponnier *et al.*, 1982, 1986]; (2) the second model favors a decoupled or at least partially decoupled crust-mantle lithosphere due to mechanically weak mid-lower crust [Royden *et al.*, 2008]. Different from the previous models with assumed vertical lithosphere rheology, a numerical modeling for surface horizontal deformation suggests that, using the GPS observed horizontal velocity alone, it is not possible to infer the lithosphere rheology at depth, nor the mechanical coupling level of the crust-mantle lithosphere [Copley, 2008].

Recent seismic observations also show competing evidence for the level of mechanical coupling. Joint analysis of seismic anisotropy from shear wave splitting and global positioning system (GPS) data suggests vertically coherent deformation of crust and mantle in SE Tibet [Sol *et al.*, 2007; Wang *et al.*, 2008]. However, seismic images of isotropic and azimuthal anisotropic shear wave speeds identify features favoring a mechanically weak zone in the mid-lower crust and show apparent depth variations of azimuthal anisotropy, which suggests the crust and mantle beneath SE Tibet deform differently [Huang *et al.*, 2010; Yao *et al.*, 2010]. Moreover, Yang *et al.* [2012] point out that strong radial anisotropy presence ( $V_{SH} > V_{SV}$ ) requires no significant partial melting to explain the midcrust low  $V_{SV}$  wave speeds, thus arguing that less weight should be put on assuming a mechanically weak zone of channel flow. Previous seismic tomographic studies offer strong evidence for mid-lower crustal low wave speed zones. Their results shed light on the crust and mantle deformation style, but further investigations with high-resolution seismic images are needed for more detailed interpretation.

Traditional ambient noise tomography requires intermediate steps of measuring dispersion curves by assuming 1D layered model between station pairs and constructing group and/or phase velocity maps. This

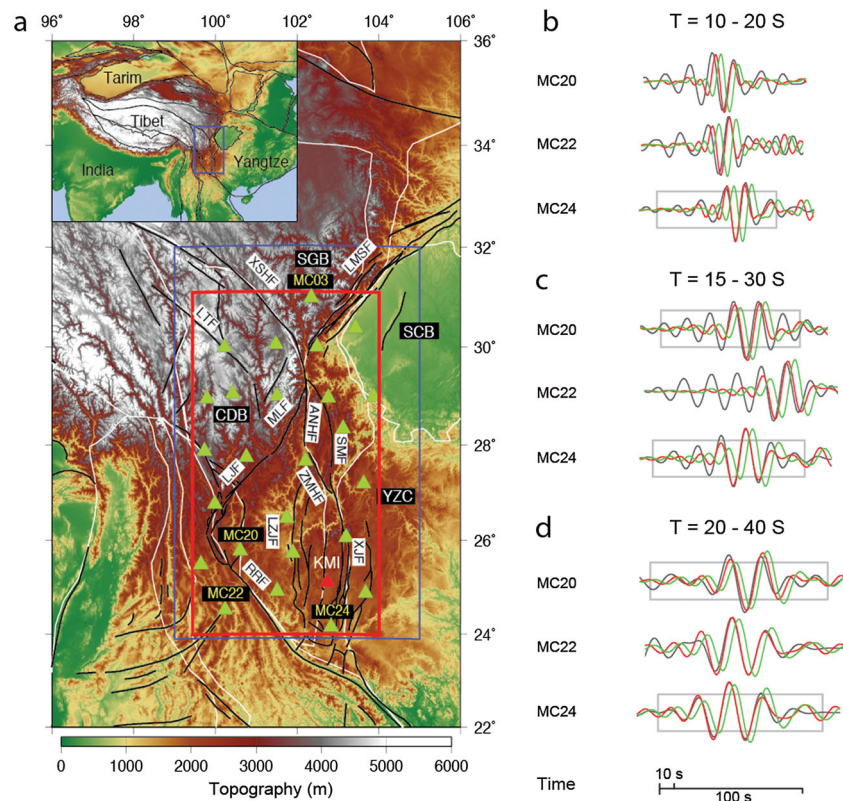


**Figure 1.** (a) Map showing topography, tectonic units, major faults, and seismic stations in SE Tibet. The inset shows the tectonic setting with tectonic unit boundaries in dark lines. The bold white lines bound the main tectonic units: SGB (Songpa-Ganze Block), CDB (Chuan-Dian Block), YZC (Yangtze Craton), and SCB (Sichuan Basin). The faults are delineated with bold dark lines and labeled in white boxes: LTF (Litang Fault), XSHF (Xianshuihe Fault), LMSF (Longmenshan Fault), MLF (Muli Fault), ANHF (Anninghe Fault), SMF (Shimian Fault), LJF (Lijiang Fault), ZMHF (Zemuhe Fault), LZJF (Luzhijiang Fault), XJF (Xiaojiang Fault), RRF (Red River Fault). The blue box indicates the adjoint tomography simulation region and the red box defines the map region in Figure 3. Green triangles mark 25 MIT array stations and red triangle the permanent station KMI. Ambient noise cross correlation of virtual source station MC03 and receiver stations (MC20, MC22, and MC24) is used to show the waveform fitting between the empirical Green's Functions (black lines) and synthetic Green's functions (SGFs) (greens lines for M00 and red lines for M13) in three period bands: (b) 10 – 20 s, (c) 15 – 30 s, and (d) 20 – 40 s. The grey boxes represent the windows selected for traveltime misfit measurement.

assumption makes the seismic imaging less accurate in terms of recovering the wave speed anomaly pattern and amplitude. Following the recent development of adjoint tomography aided by numerical methods [Tromp *et al.*, 2005, 2010; Tape *et al.*, 2009], we propose an adjoint tomography technique utilizing a spectral-element method (SEM) to assimilate vertical component empirical Green's functions (EGFs) [Shapiro and Campillo, 2004; Sabra *et al.*, 2005; Yao *et al.*, 2006]. Our goal is to refine the shear wave speed model beneath SE Tibet and to better map the connectivity of low wave speed zones in the crust. Nevertheless, spatial distribution variations of noise sources may result in different sensitivity kernels of EGF phases [Tromp *et al.*, 2010]. Yao and van der Hilst [2009] concluded that for the region under study the effect of uneven noise source distribution is small (and negligible) for traditional ambient noise tomography, and we assume that the same is true for our ambient noise adjoint tomography.

## 2. Data and Method

Displacement empirical Green's functions (EGFs) are derived from the cross-correlation functions between station pairs using the continuous vertical component ambient noise, recorded by 25 MIT array stations and one permanent station KMI (Figure 1a) [Huang *et al.*, 2010]. We compute SEM synthetic Green's functions (SGFs) using a spectral-element code [Komatitsch *et al.*, 2004], with a vertical force at 1 km depth beneath each station as virtual source, and a Gaussian function with 2.5 s half duration mimicking delta source time function. A regular mesh is implemented with 2.5 km average grid spacing, within a simulation domain of

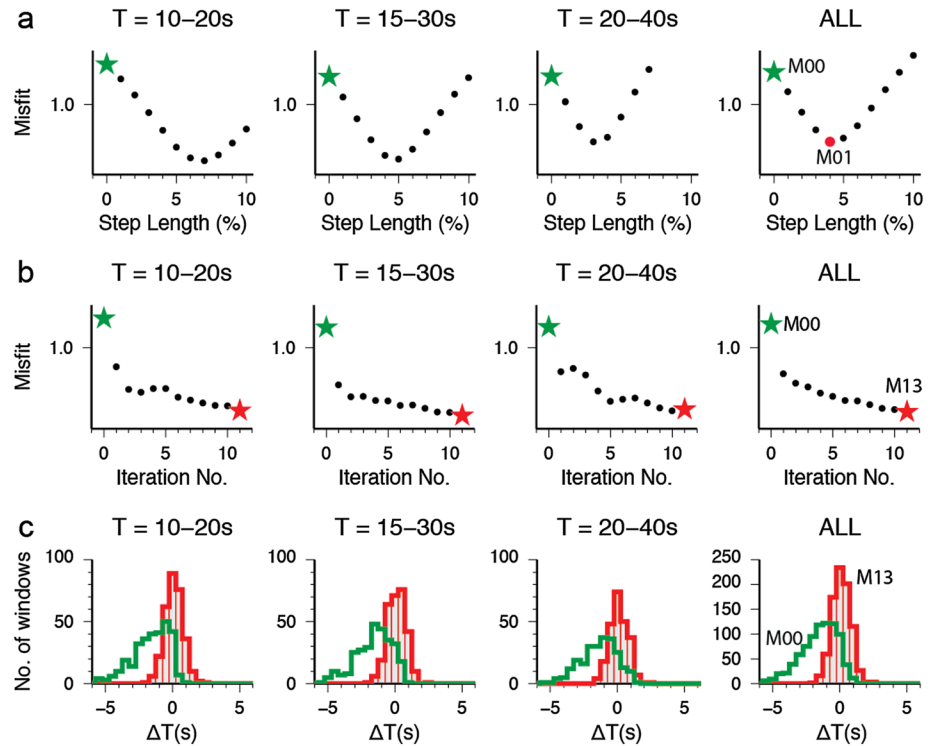


**Figure 2.** (a) Line search for updating the model from M00 (green star) to M01 (red dot). The overall weighted normalized traveltimes misfit (ALL) has contributions from three period bands. The misfit minimum (ALL) locates the optimal step length for the new model, which is 4% for M01. (b) The misfits decrease when the tomographic inversion proceeds to a higher number of iteration, not only for the overall misfits (ALL), but also for the misfits in different period bands. Green stars mark the misfits for M00, and red stars for M13 after 13 iterations. Note that the vertical axis is plotted in logarithmic scale in Figures 2a and 2b. (c) Histograms of traveltimes misfits for M00 (green lines) and M13 (red lines).

589 km × 887 km at the surface and extending to 100 km depth. The mesh also incorporates 5 km topographic variation from the Sichuan basin to the Tibetan plateau.

We then filter the EGFs and SGFs in three period bands, 10 – 20 s, 15 – 30 s, and 20 – 40 s. Filtered EGFs are normalized in amplitude to their corresponding SGFs. Automatic algorithm FLEXWIN [Maggi et al., 2009] makes the window selection for traveltimes misfit measurements (Figures 1b, 1c, and 1d). Structure parameter perturbations are directly linked to SGF-EGF traveltimes misfit function  $\chi$  through the forward and adjoint seismic-wave equations [Tromp et al., 2005] (equations (S3) and (S5), see supporting information). By minimizing the frequency-dependent  $\chi$  iteratively, we seek to improve the model with adding perturbations in structure parameters.

We start with a 3D initial model (M00, Figures S1 and S2a) produced by Yao et al. [2010] from a joint inversion of teleseismic surface waves and ambient noise derived EGFs. The initial SGFs and EGFs have reasonably good fits but show certain misfits in phase in different period bands (Figures 1b, 1c, and 1d). We determine the search direction of the next  $\chi$  minimum using Fréchet kernel  $\mathbf{g}$  modified by the preconditioner (equation (S12)) and chose the optimal model step length based on line search (Figure 2a). The same procedure is repeated until no significant further reduction of  $\chi$  is expected, which in our case occurs after 13 iterations (Figure 2b). The final 3D model (M13) shows significant improvement on SGF-EGF fits (Figures 1b, 1c, 1d, 2b, and 2c) and traveltimes misfit reduction (from the initial  $-1.53 \pm 1.34$  s to the final  $-0.12 \pm 0.67$  s) (Figure 2c), which verifies the adjoint tomography results in situ and suggests an improved 3D model compatible with the EGF observables.

### 3. Results and Discussion

Figures 3, 4b, and 4c present shear wave speed anomalies of M13 and its difference  $dM$  from M00. All the anomalies are relative to  $M_{ref}$ , a reference model with a 3D crust on top of 1D ak135 mantle. The crustal



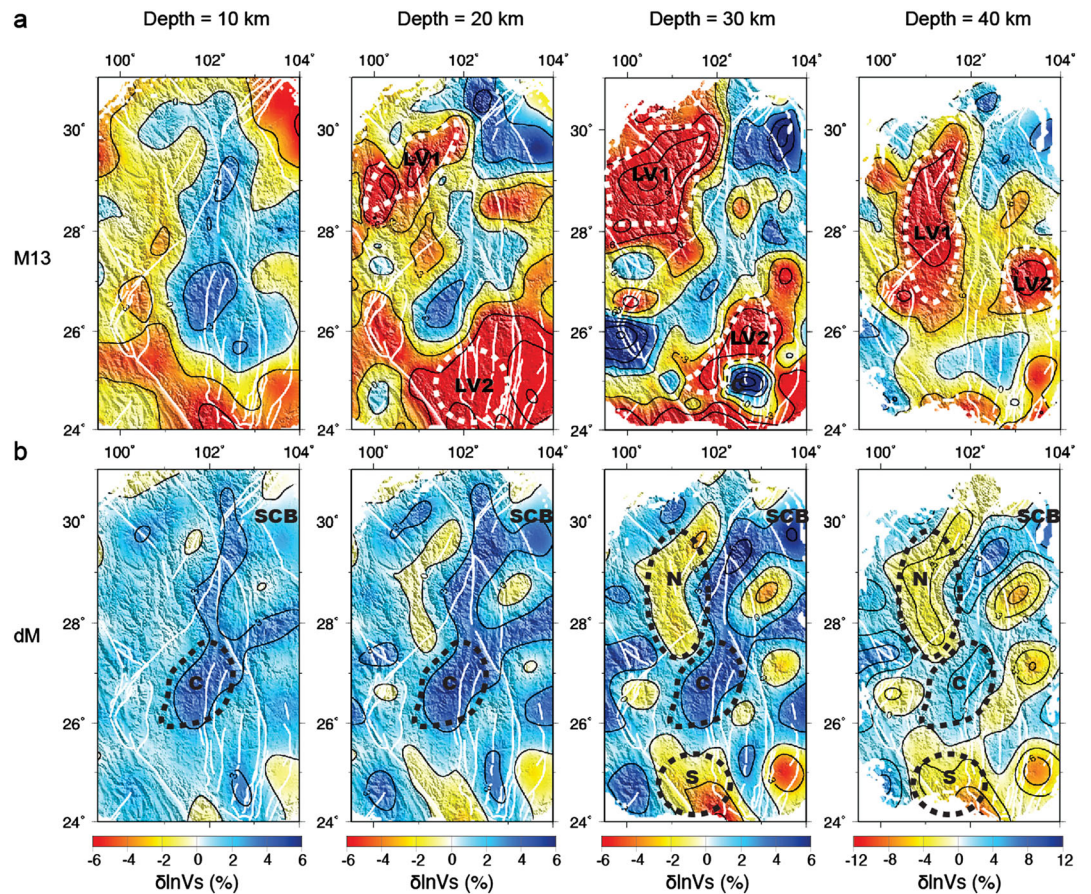


**Figure 3.** Shear wave speed anomaly maps of (a) M13 and (b) dM at 10, 20, 30, and 40 km depth, showing only for regions with enough data coverage (Figure S1), superimposed on topography gradients. The white bold lines delineate the major faults. The thin dark lines are the contour lines for wave speed anomalies. (a) The bold white dash lines bound the low wave speed patches (6 – 12% wave speed reduction), marked by LV1 and LV2. (b) The bold dark dash lines define patches in M13 (marked by N, C, and S) showing large wave speed changes compared to M00.

thickness variations are inferred from receiver functions [Xu *et al.*, 2007], and the upper, middle, and lower crust are set to about one third of the total crustal thickness, with  $V_s = 3.4, 3.6,$  and  $3.8$  km/s in each layer, respectively. Figures 3b and 4c reveal two main differences between M13 and M00: (1) 3 – 6% faster wave speed anomalies beneath SCB and the central CDB (region C in Figure 3b), the latter are bounded by Muli Fault (MLF), Lijiang Fault (LJF) and Red River Fault (RRF) to the west, and Shimian Fault (SMF) and Xiaojiang Fault (XJF) to the east; (2) 3 – 6% slower wave speed anomalies in the mid-lower crust (depth = 30 – 50 km) in the vicinity of Xianshuihe Fault (XSHF), Litang Fault (LTF), Lijiang Fault (LJF), Shimian Fault (SMF), Xiaojiang Fault (XJF), and Red River Fault (RRF) (region N and S in Figure 3b).

The lateral distribution of low wave speed zones (LV1 and LV2 in Figures 3a and 4b) beneath Xianshuihe Fault (XSHF), Litang Fault (LTF), and Xiaojiang Fault (XJF) correspond with the high electrical conductivity region (zone B) inferred from magnetotelluric data [Bai *et al.*, 2010]. Bai *et al.* [2010] propose that the crustal flow in zone B follows the major faults Xianshuihe Fault (XSHF) and Xiaojiang Fault (XJF); however, our seismic images suggest that two main low wave speed zones exist in the mid-lower crust, one along Xianshuihe Fault (XSHF), Litang Fault (LTF), Muli Fault (MLF), and Lijiang Fault (LJF) (LV1), and the other along Red River Fault (RRF) and Xiaojiang Fault (XJF) (LV2). If crustal flow regions correspond to these low wave speed zones, our results could imply different pathways of such flow.

Figure 4b shows midcrust low wave speed zones tilting downward into the lower crust and uppermost mantle beneath high wave speed regions such as SCB and the central CDB. In particular, the cross sections along profiles AA', BB', and FF' (Figure 4b) indicate that the low wave speed zone (LVZ) terminates adjacent to

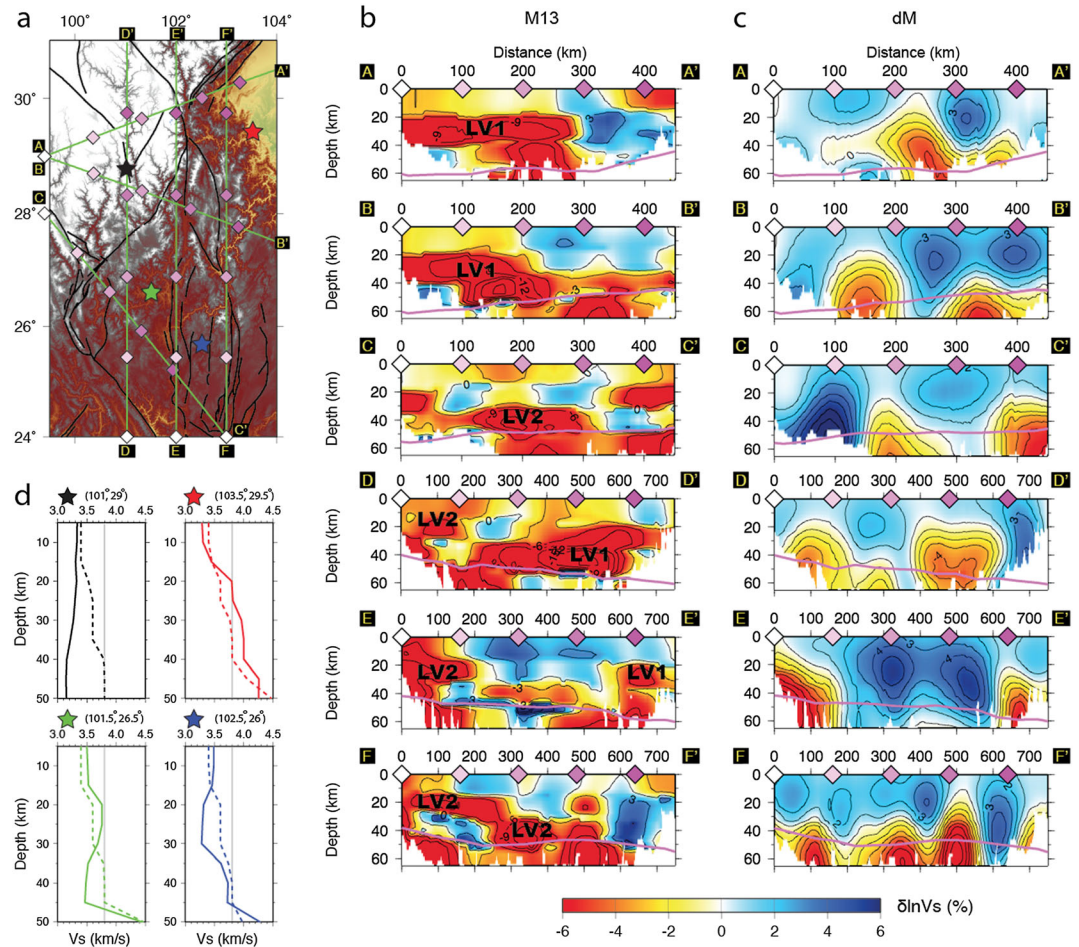


**Figure 4.** (a) Map indicating six profiles with green lines anchored by light to deep pink diamonds, with their vertical cross sections of shear wave speed anomalies shown in Figure 4b for M13 and Figure 4c for dM. LV1 and LV2 mark the low wave speed zones with 6 – 12% wave speed reduction in Figure 4b. Solid pink line denotes the Moho interface in Figures 4b and 4c. (d) One-dimensional profiles of absolute shear wave speeds (solid line — M13, dash line — Mref) for four points in different tectonic regions marked by stars in map. Grey lines in the 1D profile plots are reference line of  $V_s = 3.8$  km/s, which is the lower crust shear wave speed of Mref.

the western edge of the SCB basement, extending into the lower crust and possibly the uppermost mantle. The depth extent of LVZ also varies significantly in different regions (Figures 4a and 4d): (1) the northern CDB region (black star) has markedly LVZ in the mid-lower crust (depth = 20 – 50 km) with  $V_s = 3.1 - 3.3$  km/s; (2) the central CDB (green star) has LVZ only in the lower crust (depth = 35 – 45 km) with  $V_s = 3.4$  km/s compared the normal lower crust  $V_s = 3.8$  km/s; (3) the southern CDB (blue star) possesses LVZ in the midcrust (depth = 20 – 30 km) with  $V_s = 3.3$  km/s, compared the normal midcrust  $V_s = 3.6$  km/s; (4) the LVZ is absent in SCB (red star), except at shallower depths (<15 km), where  $V_s$  is low due to sedimentary deposits inside the basin.

Seismic and magnetotelluric imaging studies have detected a widespread crustal LVZ in the Southern and SE Tibet, which was explained by partial melt and/or aqueous fluid [Yao *et al.*, 2008; Caldwell *et al.*, 2009; Bai *et al.*, 2010]. Bai *et al.* [2010] suggest that 5 – 20% fluid content accounts for the observed high conductivity in zone B given a 20 km thick conductor. Alternatively, based on the laboratory experiments by Takei [2000], the shear wave speed ( $V_{SV}$ ) reduction of 6 – 12% from this study implies the presence of 2.5 – 5% melt beneath SE Tibet, although with the caveat that the strong radial anisotropy presence ( $V_{SH} > V_{SV}$ ) can lead to less reduced voigt-averaged shear wave speed  $V_s$ , and thus requires less pervasive midcrust partial melts [Yang *et al.*, 2012; Xie *et al.*, 2013]. In particular, Xie *et al.*'s study [2013] shows no compelling evidence of  $V_s$  being less than 3.4 km/s, a proxy for the onset of partial melting, pervasively across all of eastern Tibet, although highly probable in disjoint regions. And among which, north Chuandian terrane coincides with the observed LV1 in our study (Figures 3a, 4b, and S2b).



Lower crust channel flow model has been used to explain the steep topography adjacent to the SCB (strong foreland), and the low-gradient topographic slope for the rest of the eastern plateau margin (weak foreland) [Clark and Royden, 2000]. Our results indicate that LVZs have more complex geometry than the horizontally pervasive but vertically confined narrow zone suggested by the channel flow models. Moreover, the LVZs in our final images are isolated regions separated by high wave speed regions, such as the root of the SCB craton and the rigid central CDB (Figures 3a, 4b, and S2b).

The observed low and high wave speed anomalies are reasonably resolved features (Figures S3, S4, S5, and S6). The correlation between major fault zones and regions with sharp wave speed contrast is still somewhat tentative owing to limited spatial resolution afforded by the data used here. At 20 km and 30 km depths, the strong-wave speed-contrast regions coincide with some major fault traces such as Xianshuihe Fault (XSHF), Muli Fault (MLF), and the Lijiang Fault (LJF) (Figures 3a and 4b). This wave speed contrast and fault trace correlation does not persist at larger depths, which could suggest complicated 3D fault interfaces at deeper depths, or partial decoupling between the upper crust and deeper lithosphere deformation beneath SE Tibet.

#### 4. Conclusions

With adjoint tomography technique aided by SEM, we are able to refine the 3D crustal model beneath SE Tibet using EGFs from the ambient noise data. The new model reveals channel like (~ 20 km thick) LVZs (6–12% wave speed reduction) in the midcrust, connecting downward with more broadened LVZ pattern in the lower crust and uppermost mantle, adjacent to the high wave speed SCB craton root and central CDB. Our results suggest crustal flow with complex spatial variations, bypassing stable regions such as SCB and the central CDB. Although it is commonly proposed that aqueous fluids and partial melts are the cause of midcrust LVZ, weakening of the lower crust could be associated with mantle upwelling, for example, beneath the Red River Fault system and the South China Sea [Li and van der Hilst, 2010], or alternatively interplay between crustal flow and mantle upwelling. Further studies of high-resolution continental scale tomography and lateral and radial variations of anisotropy will help to understand better the origin of low wave speed zones at deeper depths and their impact on the deformation style of SE Tibet.

#### Acknowledgments

We thank Rice Research Computing Support Group. This work is supported by XSEDE research allocation TG-EAR130011, EAR0910618, TG-EAR130022, NSF0748455, NSFC41222028, and NSFC41274099. This research is also supported by the Chinese Academy of Sciences / State Administration of Foreign Experts Affairs International Partnership Program for Creative Research Teams.

The Editor thanks two anonymous reviewers for assistance in evaluating this manuscript.

#### References

- Bai, D., et al. (2010), Crustal deformation of the eastern Tibetan plateau revealed by magnetotelluric imaging, *Nat. Geosci.*, 3(5), 358–362, doi:10.1038/ngeo830.
- Caldwell, W. B., S. L. Klemperer, S. S. Rai, and J. F. Lawrence (2009), Partial melt in the upper-middle crust of the northwest Himalaya revealed by Rayleigh wave dispersion, *Tectonophysics*, 477, 58–65, doi:10.1016/j.tecto.2009.01.013.
- Clark, M. K., and L. H. Royden (2000), Topographic ooze: Building the eastern margin of Tibet by lower crustal flow, *Geology*, 28(8), 703–706.
- Copley, A. (2008), Kinematics and dynamics of the southeastern margin of the Tibetan Plateau, *Geophys. J. Int.*, 174(3), 1081–1100, doi:10.1111/j.1365-246X.2008.03853.x.
- Huang, H., H. Yao, and R. D. van der Hilst (2010), Radial anisotropy in the crust of SE Tibet and SW China from ambient noise interferometry, *Geophys. Res. Lett.*, 37, L21310, doi:10.1029/2010GL044981.
- Komatitsch, D., Q. Liu, J. Tromp, P. Su, C. Stidham, and J. H. Shaw (2004), Simulations of ground motion in the Los Angeles Basin Based upon the spectral-element method, *Bull. Seismol. Soc. Am.*, 94(1), 187–206.
- Li, C., and R. D. van der Hilst (2010), Structure of the upper mantle and transition zone beneath Southeast Asia from traveltimes tomography, *J. Geophys. Res.*, 115, B07308, doi:10.1029/2009JB006882.
- Maggi, A., C. Tape, M. Chen, D. Chao, and J. Tromp (2009), An automated time-window selection algorithm for seismic tomography, *Geophys. J. Int.*, 178(1), 257–281, doi:10.1111/j.1365-246X.2009.04099.x.
- Royden, L. H., B. C. Burchfiel, and R. D. van der Hilst (2008), The geological evolution of the Tibetan Plateau, *Science*, 321, 1054–1058, doi:10.1126/science.1155371.
- Sabra, K. G., P. Gerstoft, P. Roux, and W. A. Kuperman (2005), Extracting time-domain Green's function estimates from ambient seismic noise, *Geophys. Res. Lett.*, 32, L03310, doi:10.1029/2004GL021862.
- Shapiro, N. M., and M. Campillo (2004), Emergence of broadband Rayleigh waves from correlations of the ambient seismic noise, *Geophys. Res. Lett.*, 31, L07614, doi:10.1029/2004GL019491.
- Sol, S., et al. (2007), Geodynamics of the southeastern Tibetan Plateau from seismic anisotropy and geodesy, *Geology*, 35(6), 563–566, doi:10.1130/G23408A.1.
- Takei, Y. (2000), Acoustic properties of partially molten media studied on a simple binary system with a controllable dihedral angle, *J. Geophys. Res.*, 105(B7), 16,665–16,682, doi:10.1029/2000JB900124.
- Tape, C., Q. Liu, A. Maggi, and J. Tromp (2009), Adjoint tomography of the southern California crust, *Science*, 325, 988–992, doi:10.1126/science.1175298.
- Tapponnier, P., G. Peltzer, A. Y. Le Dain, R. Armijo, and P. Cobbold (1982), Propagating extrusion tectonics in Asia: New insights from simple experiments with plasticine, *Geology*, 10, 611–616, doi:10.1130/0091-7613(1982)10<611>
- Tapponnier, P., G. Peltzer, and R. Armijo (1986), On the mechanics of the collision between India and Asia, *Geol. Soc. London, Spec. Publ.*, 19(1), 113–157, doi:10.1144/GSL.SP.1986.019.01.07.
- Tromp, J., C. Tape, and Q. Liu (2005), Seismic tomography, adjoint methods, time reversal and banana-doughnut kernels, *Geophys. J. Int.*, 160(1), 195–216, doi:10.1111/j.1365-246X.2004.02453.x.

- Tromp, J., Y. Luo, S. Hanasoge, and D. Peter (2010), Noise cross-correlation sensitivity kernels, *Geophys. J. Int.*, *183*(2), 791–819, doi:10.1111/j.1365-246X.2010.04721.x.
- Wang, C.-Y., L. M. Flesch, P. G. Silver, L.-J. Chang, and W. W. Chan (2008), Evidence for mechanically coupled lithosphere in central Asia and resulting implications, *Geology*, *36*(5), 363, doi:10.1130/G24450A.1.
- Xie, J., M. H. Ritzwoller, W. Shen, Y. Yang, Y. Zheng, and L. Zhou (2013), Crustal radial anisotropy across Eastern Tibet and the Western Yangtze Craton, *J. Geophys. Res. Solid Earth*, *118*, 4226–4252, doi:10.1002/jgrb.50296.
- Xu, L., S. Rondenay, and R. D. van der Hilst (2007), Structure of the crust beneath the southeastern Tibetan Plateau from teleseismic receiver functions, *Phys. Earth Planet. Inter.*, *165*(3–4), 176–193, doi:10.1016/j.pepi.2007.09.002.
- Yang, Y., M. H. Ritzwoller, Y. Zheng, W. Shen, A. L. Levshin, and Z. Xie (2012), A synoptic view of the distribution and connectivity of the mid-crustal low velocity zone beneath Tibet, *J. Geophys. Res.*, *117*, B04303, doi:10.1029/2011JB008810.
- Yao, H., R. D. van der Hilst, and M. V. de Hoop (2006), Surface-wave array tomography in SE Tibet from ambient seismic noise and two-station analysis - I. Phase velocity maps, *Geophys. J. Int.*, *166*(2), 732–744, doi:10.1111/j.1365-246X.2006.03028.x.
- Yao, H., C. Beghein, and R. D. van der Hilst (2008), Surface wave array tomography in SE Tibet from ambient seismic noise and two-station analysis - II. Crustal and upper-mantle structure, *Geophys. J. Int.*, *173*(1), 205–219, doi:10.1111/j.1365-246X.2007.03696.x.
- Yao, H., and R. D. van der Hilst (2009), Analysis of ambient noise energy distribution and phase velocity bias in ambient noise tomography, with application to SE Tibet, *Geophys. J. Int.*, *179*(2), 1113–1132, doi:10.1111/j.1365-246X.2009.04329.x.
- Yao, H., R. D. van der Hilst, and J.-P. Montagner (2010), Heterogeneity and anisotropy of the lithosphere of SE Tibet from surface wave array tomography, *J. Geophys. Res.*, *115*, B12307, doi:10.1029/2009JB007142.